Chemical Physics Impact 6 (2023) 100221

Contents lists available at ScienceDirect

Chemical Physics Impact

journal homepage: www.sciencedirect.com/journal/chemical-physics-impact

Investigation of the site-specific binding interactions and sensitivity of ochratoxin with aluminum nitride ($Al_{12}N_{12}$) nanoclusters. An intuition from Quantum Chemical Calculations

Ernest C. Agwamba [a,b,*], Hitler Louis [a,c], Innocent Benjamin [a,*], Ernest E. Ekereke [a], Gideon E. Mathias [a,c], Eze F. Ahuekwe [a,d], Adedapo S. Adeyinka [e]

[a] Computational and Bio-Simulation Research Group, University of Calabar, Calabar, Nigeria
[b] Department of Chemistry, Covenant University Ota, Nigeria
[c] Department of Pure and Applied Chemistry, Faculty of Physical Sciences, University of Calabar, Calabar, Nigeria
[d] Department of Biological Sciences, Covenant University Ota, Nigeria
[e] Department of Chemical Sciences, Research Centre for Synthesis and Catalysis, University of Johannesburg, South Africa

ARTICLE INFO

Keywords:
Ochratoxin
DFT
AlN
Adsorption energy
Sensor
Aluminiuim nitride
Nanocluster

ABSTRACT

Density functional theory (DFT) computing was used in this study to examine the feasibility for detecting the interaction of nitrogen (Ochra@AlN...N), oxygen (Ochra@AlN...O), and chlorine (Ochra@AlN...Cl) with the surface of an aluminum nitride ($Al_{12}N_{12}$) nanocluster. The DFT/PBE0-D3/aug-cc-pVDZ approach was heavily utilised in the computations of the quantum electronic structural characteristics, interaction energies, and sensing parameters. Fascinatingly, the results showed that Ochra@AlN...O, with a value of 2.04 eV, possessed a higher energy gap, making it the most stable among the spatial orientations. Meanwhile, Ochra@AlN...Cl had the lowest energy gap of 1.55 eV, making it the least stable and more reactive compound. More so, the natural bond analysis (NBO) analysis indicated that Ochra@AlN...O has the highest energy of perturbation among adsorption atoms. However, a decrement was observed in the energy value for Ochra@AlN...Cl, Ochra@AlN...N, and Ochra@AlN...O with energy values of 1.55, 1.82, and 2.04 eV, respectively, compared to the energy gap value of 2.37 eV of the Al12N12 nanocluster. Also, the adsorption study showed that Ochra@AlN...O interaction had the greatest negative adsorption energy of -2.466 eV and thus, possesses the fastest recovery time of 3.3E-158 s. The recovery time for Ochra@AlN...N was 1.6E-156 s, and the least responsive was Ochra@AlN...Cl with a recovery time of 1.94E-86. Ochra@AlN...Cl indicated the fastest response with a time of 1.616 s, followed by 1.757 s for Ochra@AlN...N, and the least responsive was Ochra@AlN...O with 1.881 s. Thus, it can be inferred that Ochra@AlN...O is the most preferred spatial orientation and interaction site of ochratoxin upon interaction with the AlN surface due to its high adsorption energy, stability, perturbation energy, and recovery time. Using the aforementioned method, this study provides valuable insights into the interactions of Ochra with the AlN surface and its potential as a sensing material.

1. Introduction

Ochratoxins are among the most significant mycotoxins produced by ochratoxigenic fungi including *Penicillium, Aspergillus, Fusarium, Alternaria, Trichoderma,* and *Trichotheium* species [1,2]. Tasic and Tasic [3] have reported pre- and post-harvest ochratoxin infections alongside isocladosporium, ergot alkaloids, cladosporin and emodin mycotoxins produced by Cladosporium species. Mycotoxins are the toxic secondary metabolites of fungi produced on a wide range of consumable substrates in temperate climates [4]. They are odourless, tasteless and colorless compounds that occur sporadically in nature [5]. Their presence affects the quality of foodstuff, and leads to the development of various diseases in consumers, termed mycotoxicoses [4,6]. Nephrotoxic, immunotoxic, teratogenic and carcinogenic impacts of ochratoxins to a variety of laboratory animals have also been reported [7,8]. Closest to these are the highly toxic and potentially carcinogenic aflatoxins which naturally co-occur with ochratoxins in spices [9]; and are produced by *A. flavus, A. parasiticus* and *A. nomius* on spices, due to their processing,

* Corresponding authors at: Computational and Bio-Simulation Research Group, University of Calabar, Calabar, Nigeria.
E-mail addresses: ernest.agwamba@gmail.com (E.C. Agwamba), benjamininnocent53@gmail.com (I. Benjamin).

https://doi.org/10.1016/j.chphi.2023.100221
Received 8 March 2023; Received in revised form 8 April 2023; Accepted 5 May 2023
Available online 14 May 2023

environmental and storage conditions [10,11]. They both attract a great concern due to their adverse effects and agroeconomic significance, accounting for millions of dollars in annual losses worldwide [12]. Tiffany, [13] submits that about 25% of the crops globally are contaminated by mycotoxins, and around 4.5–5.0 billion individuals are at risk of chronic mycotoxins exposure. Risky foods such as dairy products, cereals, cocoa, coffee, grapevine, dried fruits and various spices remain the culprit ochratoxins exposure routes to humans [14]. As such, the IARC has classified O ochratoxins A (OTA) as a probable human carcinogen (Group 2B) based on sufficient evidence for carcinogenicity in animal and human studies [15].

Studies on the qualitative and quantitative detection of ochtratoxins with traditional chromatographic methods abound. Ozbey and Kabak, [9] investigated the natural co-occurrence of aflatoxins and OTA in spices employed widely in the preparation of processed foods in Turkey, using high-performance liquid chromatography with fluorescence detection (HPLC-FD) after immunoaffinity column (IAC) clean-up. There are reports of qualitative and quantitative detection of ochratoxins by enzyme linked immunosorbent assay (ELISA), and further confirmation with liquid chromatography–tandem mass spectrometric (LC-MS-MS) in Indian spices [7]; and in Chinese medicine by LC-MS-MS [16]. Lasram et al. [17] extracted ochratoxins from Tunisian red chili powder using immunoaffinity columns and quantified by High Performance Liquid Chromatography (HPLC). Similarly, Jalili and Jinap, [7] and Zareshahrabadi et al. [18] analyzed ochratoxins using a high-performance liquid chromatographic-fluorescence detector (HPLC-FD), while Naeem et al. [1] conducted further chemical analysis for the best fraction via Gas Chromatography-Mass Spectroscopy (GC–MS). These approaches present ochratoxin detection limits at levels beyond legislation limits of >15 μg/kg [18]. Thus, necessitating effective quality control procedures and empowerment of food-related laboratories with precise methods of ochratoxin detection.

In light of this, the aluminum nitride (AlN) nanocage sensors and doped derivatives offer a viable and highly sensitive approach owing to their exceptional characters, which include high surface/volume ratio and sensitive electronic properties [19–21]. Kumar et al. [22] had highlighted the use of nanomaterials on diverse sensing principles, with advanced nanomaterial-based biosensors (and improved ELISA-based nanomaterials) recently being fabricated for point-of-care clinical diagnosis [23], environmental monitoring, and food safety [24]. Applications of these functional nanomaterials currently include their use as environmental adsorbents, sensors, antibacterial materials, and sharp memory materials [25–27]. Doping as an important and effective method for improving the sensing properties changes the substrate-sensing properties of the semiconductor nanoparticles by altering its energy band structure and morphology. Thus, creating more centres for substrate interaction on the metal oxide semiconductor nanoparticles surface [28,29]. Aluminum nitride (AlN), as a complementary metal-oxide semiconductor (CMOS)-compatible material has a wide bandgap of 6.2 eV, a broad transparency window covering from ultraviolet (UV) to mid-infrared (MIR), and a significant second-order nonlinear optical effect. These attributes aid in overcoming the limitations of indirect bandgap of 1.1 eV, transparency wavelength of >1.1 μm, and insignificant second-order nonlinear optical property of natural CMOS, like silicon [30,31]. As such, it makes for their potential application in many areas like communication [32], optical ranging [33], bio/chemical sensing [34,35], computing [36], and quantum information processing [37].

Recently, Wei and Liu, [19] prepared Al-doped nitride nanocage for the adsorption of ibuprofen through electrostatic mechanism in both water and gas phases. They demonstrated a significant AIN HOMO-LUMO gap decrease after ibuprofen adsorption, submitting that the AlN nanocage would serve as a function-type sensor selectively identifying the ibuprofen molecule in the presence of environmental pollutants. More so, Zhang et al. [38] demonstrated the function-type sensor capacity of AlN nanocage for acetaminophen detection in the presence of methanol and other pollutants. Several authors have tried to elucidate the adsorption behavior and electronic response of AlN nanotube and nanocage via quantum chemical density functional theory (DFT) calculations in various sensor applications. DFT calculations have wholistically become popular for the investigation of suitable sensor materials as well as evince other electronic properties. These include detections for halothane gas [39], anticancer drug [40], arsine gas [41], and in Li-ion batteries [42]; with Seif et al. [43] previously reporting a DFT calculation of the electric field gradient (EFG) sensors at the sites of aluminum and nitrogen nuclei. In this study, DFT was utilized to calculate the electronic structure and energetics of the ochratoxin and $Al_{12}N_{12}$ clusters' binding interactions, thus providing a better understanding of the binding mechanism. It is worth mentioning that DFT helps to predict the distribution of electron density in molecules and solids, providing insights into the molecular structures and chemical properties of materials. Furthermore, DFT was also explored to evaluate various theoretical parameters such as bond length, which are critical in predicting the reactivity and sensitivity of the ochratoxin and $Al_{12}N_{12}$ clusters. The insights gained from DFT calculations seeks to design and develop new materials with desirable properties [44–47] that could detect ochratoxin. To effectively study the interaction between these molecules, density functional theory approach was utilized at PBE0/aug-cc-pvdz computational method.

2. Computational method

All geometry optimization was performed in this work within the circumference of density functional theory using GaussView 6.0.16 and Gaussian 16 software [48]. Ground-state structural analysis was carried out using the perdew-Burke-Ernzehof (PBE0) functional with the aug-cc-pvdz method [49]. To select the appropriate DFT approach, it is important to consider the atomization energies of the constructed systems and how the atomization energies can be improved for a large database of small complexes, as well as capturing the minute atomic interactions. In an attempt to meet this need, the above level of computational theory was employed. All the optimized files generated from Gaussian 16 software were visualized using the chemcraft program v1.6. The natural bond orbital (NBO) calculation was conducted using the NB03.1 software [50], embedded in the Gaussian program. Multiwfn software [51], originpro [52], and visual molecular dynamics (VMD), which are all excellent molecular graphics software, were optimally utilized to conduct QTAIM, molecular orbital visualization, density of state (DOS), and Recovery/Response time of the adsorbate and adsorbent species with respect to their different interaction sites. To effectively evaluate the adsorption energies of the isolated complexes, Eq. (1) [53–55] was employed to calculate the exact adsorption energies involved and carefully compared with the obtained calculated thermodynamic stability of the interacting species to probe the feasibility of the interaction process.

The highest occupied molecular orbital (HOMO) and lowest unoccupied molecular orbital (LUMO) was used to determine the energy gap of the studied compounds defined in Eq. (1).

$$\mathrm{Egap(eV)} = \mathrm{ELUMO\ (eV)} - - \mathrm{EHOMO\ (eV)} \quad (1)$$

Where ELUMO (eV) is the energy of the LUMO, EHOMO (eV) is the energy of the HOMO, and Egap is the energy gap, all in electron volts. The quantum chemical descriptors, including chemical hardness (η), global softness (σ), chemical potential (μ), and electrophilicity index (ω), were exhaustively utilized by applying Koopman's theorem [56], Eqs. (2) to (5). All results computed for the second-order stabilization energy are presented in Table 5 and were extracted based on the highest E2 values, with E2 expressed mathematically as Eq. (6). The adsorption energies for the studied interactions have also been calculated using Eq. (7), with consideration given to the basic set superposition error (BSSE). The values of the calculated adsorption energy for the respective interactions are presented in Table 1. The RDG analysis is calculated by

Table 1
The calculated adsorption energies in atomic units (au) and electron Volt (eV) for the three systems.

Interactions	@Chlorine Interaction	@Nitrogen Interaction	@Oxygen Interaction
Adsorption Energy (a.u)	−0.0681	−0.044	−0.0906
Adsorption Energy (eV)	−1.8534	−1.1973	−2.4658
BSSE (eV)	0.0005	0.0156	0.0130
$Ead_{corrected}$ (eV)	−1.8390	−0.7730	−2.1121
Enthalpy of Adsorption $\Delta_f H^0$ (kcal/mol)	−98.95	−38.29	−97.19
Entropy of Adsorption (S) (kcal/mol)	0.28	0.28	0.27
Gibbs free energy of formation ΔrG^0 (kcal/mol)	−19.80	−23.85	−82.0814
Solvation energy (kcal/mol)	−26.02	−25.57	−28.29

employing Eq. (8).

$$\eta = \frac{E_{HOMO} - E_{LUMO}}{2} \tag{2}$$

$$\sigma = \frac{1}{2\eta} = \frac{1}{E_{HOMO} - E_{LUMO}} \tag{3}$$

$$\mu = \frac{E_{HOMO} + E_{LUMO}}{2} \tag{4}$$

$$\omega = \frac{\mu^2}{2\eta} \tag{5}$$

$$\mathrm{E2} = \Delta \mathrm{Eij} = \mathrm{qi}\ \frac{F(i,j)^2}{\varepsilon_j - \varepsilon_i} \tag{6}$$

$$E_{ads} = E_{COMPLEX} - -(E_{SURFACE} + E_{GAS}) + BSSE \tag{7}$$

$$RDG = \frac{1}{2(3\pi^2)^{\frac{1}{3}}} \frac{|\overline{\Delta\rho}(\mathbf{r})|}{\overline{\rho(\mathbf{r})}^{\frac{4}{3}}} \tag{8}$$

For Eq. (8), q_i is the donor orbital occupancy, ε_j, ε_i are the diagonal elements of (orbital energies), F_{ij} is the off-diagonal NBO Fock Matrix element. Also, for Eq. (7), $E_{COMPLEX}$ is the energy of the complex, $E_{SURFACE}$ is the energy of the surface and E_{GAS} represent the energy of the gas respectively. Also, for Eq. (8), ρ(r) and ∇ρ(r)stand for the electron density and gradient of the electron density.

3. Results and discussion

3.1. Geometry and structural analysis

The selected bond distances and bond angles for the optimized geometry of the studied interactions were carried out using the GaussView program, employing the DFT/PBE0/ aug-cc-pvdz level of theory. The selected bond distances and angles are presented in Table S1 of the supporting information for the aluminum nitride surface and Table S2 for the molecule after interaction with Ochratoxin. It can be deduced from Table S1 that the bond distances around the studied surface (AlN) are identical, with bond distances N1-Al_{17} (1.9336 Å), N_1-Al_{23} (1.9336 Å), N_9-Al_{18} (1.9020 Å), Al_{14}-Al_{19} (2.4704 Å), and Al_{15}-Al_{22} (2.4699 Å). The selected bond angles for the aluminum nitride surface also have equal bond angles, as observed in Table S1, with N_1-Al_{24}-N_{10} having a bond angle of 130.400°, N_5-Al_{13}-N_6 with a bond angle of 130.4180°, N_6-Al_{13}-N_8 with a bond angle of 95.8430°, N_7-Al_{19}-Al_{18} with a bond angle of 115.170°, and Al_{14}-Al_{18}-Al_{24} with a bond angle of 113.9130°, respectively.

After interacting the aluminum nitride surface with Ochra, the obtained bond distance is observed to be relatively smaller than the bond distances observed when it was interacted with chlorine, nitrogen, and oxygen atoms. The observed bond distances, as presented in Table S2 of the supporting information, show that the bond distance for C1-C2 follows an increasing order of Ochra (1.395 Å) < Ochra@AlN..N (1.40428 Å) < Ochra@AlN..Cl (1.40506 Å) < Ochra@AlN..O (1.41725 Å), with a mean bond distance of 1.40541 Å. The bond distance for C10-N39 follows an increasing order of Ochra (1.36905 Å) < Ochra@AlN..Cl (1.33981 Å) < Ochra@AlN..O (1.36754 Å) < Ochra@AlN..N (1.44956 Å), with a mean bond distance of 1.38149 Å. For the bond distance of C_{17}-Cl_{46}, a similar pattern is observed, with Ochra (1.71974 Å) < Ochra@AlN..N (1.75945 Å) < Ochra@AlN..O (1.76654 Å) < Ochra@AlN..Cl (1.77376 Å), with a mean bond distance of 1.75487 Å. For C14-C20, the observed bond distances after interaction follow an increasing order of Ochra (1.39506 Å) < Ochra@AlN..N (1.42134 Å) < Ochra@AlN..Cl (1.42156 Å) < Ochra@AlN..O (1.46206 Å), with a mean bond distance of 1.42501 Å. Finally, the bond distance for C20-O45 is observed to follow an increasing pattern of Ochra (1.355 Å) < Ochra@AlN..O (1.281 Å) < Ochra@AlN..N (1.3410 Å) < Ochra@AlN..Cl (1.342 Å), with a mean bond distance of 1.3297 Å. Following the trend of results in the bond distances, it is observed that the interaction Ochra@AlN..N has shorter bond distances followed by Ochra@AlN..O and Ochra@AlN..Cl, respectively. Visualization of the optimized AlN nanocage after interaction with Ochra@Cl, Ochra@N and Ochra@O is depicted as Fig. 2.

3.2. Different adsorption configurations of ochratoxin on $Al_{12}N_{12}$ nanocage

To ascertain the most stable adsorption configurations, different orientations of Ochratoxin on the aluminum nitride (AlN) nanocage were explored. From these orientations, three different adsorption sites have been identified and visualized in Fig. 2. Each adsorption site on the Ochratoxin molecule was found on the Chlorine, Nitrogen, and Oxygen atoms, denoted as site 1, 2, and 3, respectively, in Fig. 2. The calculated adsorption energies obtained from different adsorption configurations, indicated as site 1 (on Chlorine), site 2 (on Nitrogen), and site 3 (on Oxygen), are shown in Table 1 with units of measurement in atomic units (a.u) and electron volts (eV). Therefore, it can be deduced that the adsorption energy is the most essential mechanism for sensing that provides important clues on the adsorption of any adsorbate on the adsorbent material via the indicator: EAd < 0 or EAd > 0, denoting chemisorption and physisorption phenomena. The greater the negative values of the adsorption energy, the better its sensing ability [57]. It can also be observed from Table 1 that the adsorption energies calculated for the interactions, considering the basic set superposition error (BSSE) formed in the different systems, follow an increasing trend of: N1 < C1 < O1, corresponding to the adsorption energies of −0.7730 eV < −1.8390 eV < −2.1121 eV. From this investigation, it can be categorically reported that the least and greatest adsorption energies are in N1 and O1 interactions, respectively. This implies that the O1 interaction of site 1, with the greatest adsorption energy, portrays better sensing performance than interactions obtained from site 1 and site 2 in the adsorption of the Ochratoxin molecule on the Aluminum nitride nanocage. In all cases, the adsorption phenomena are best described as chemisorption (Fig. 1).

3.3. Solvation energy

Using the polarizable continuum model (PCM), this study investigated the polar (water) solvent influence on the interaction between ochratoxin and Cl, N, and O doped clusters of AlN. To this effect, the structural systems were again reoptimized in the solvent and tabulated the calculated parameters as shown in Table 1. The stability of the investigated complexes in the solvents (water) is confirmed with the negative values for the solvation energies ($E_{solv.}$) calculated utilizing Eq.

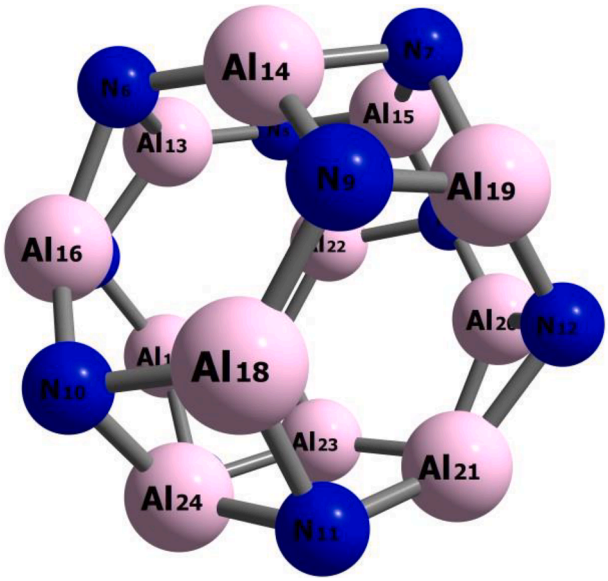

Fig. 1. Optimized AlN Nanocage Structure Investigated at the DFT/PBE0 Method with aug-cc-pvdz Basis Set for Interactions with Ochra@C, Ochra@N, and Ochra@O Molecules.

(9).

$$E_{solv} = E_{T.sol} - E_{gas} \tag{9}$$

where the $E_{T.sol}$ represents the total energy of the system in the solvent phase, and E_{gas} represents the total energy of the system in the gaseous phase. As can be seen from the results obtained, the solvation energy of the decorated clusters increased on adsorption of ochratoxin. Overall, the energy values are maximum in the gas phase and minimum in water which confirms their solubility in the polar solvent compared to the gas phase and their ability to sense ochratoxin efficiently. Substantially, in their other of superiority, it can be reported that AIN-Ochra@O inarguably demonstrates more solubility potentials in water (−28.29 kcal/mol) than AIN-Ochra@Cl and AIN-Ochra@N. It is worth mentioning that the effect of solvation in the studied systems greatly agrees with the adsorption energies earlier discussed.

3.4. Reactivity and stability descriptors

The highest occupied molecular orbital (HOMO), lowest unoccupied molecular orbital (LUMO), and energy gap (Egap) are all reported in electron volts (eV) [58] for the studied molecules. The electronic properties, such as the global descriptor parameters, were calculated to understand the stability and reactivity of the studied molecules [59]. The stability and reactivity of the studied compounds Ochra@AlN..Cl, Ochra@AlN..N, and Ochra@AlN..O were obtained from the results. It was divulged that upon the interaction of Ochra on the surface of AlN, a slight drift in the stability of the complexes was observed, which could be attributed to the various interaction sites of the investigated molecules. The results further explicated that the adsorption of ochra on the aluminum nitride nanocluster influenced the nucleophilicity, electrophilicity, and stability of the studied complex before and after interaction. As such, the energy gap, which is obtained from the difference in the energy value of the HOMO and LUMO for the adsorbed compounds, was observed to follow a decreasing trend from 2.37 eV to 1.55 eV. However, it is evident that the Ochra@AlN..Cl interaction is likely to be unstable, as elucidated by the low energy gap of 1.55 eV. Meanwhile, the results explicated that the stability of the molecule was applauded upon interaction via the oxygen site at Ochra@AlN..O compound with an energy gap of 2.04 eV, suggesting that the aforementioned compound is likely to possess a comparably high interaction process as well as stability potency with a high tendency to release electrons. Before the adsorption of Ochra gas, the AIN surface was observed to possess an energy gap of 2.37 eV, which is comparatively higher than the energy gap of 2.23 eV observed for Ochratoxin gas. The visualization of the

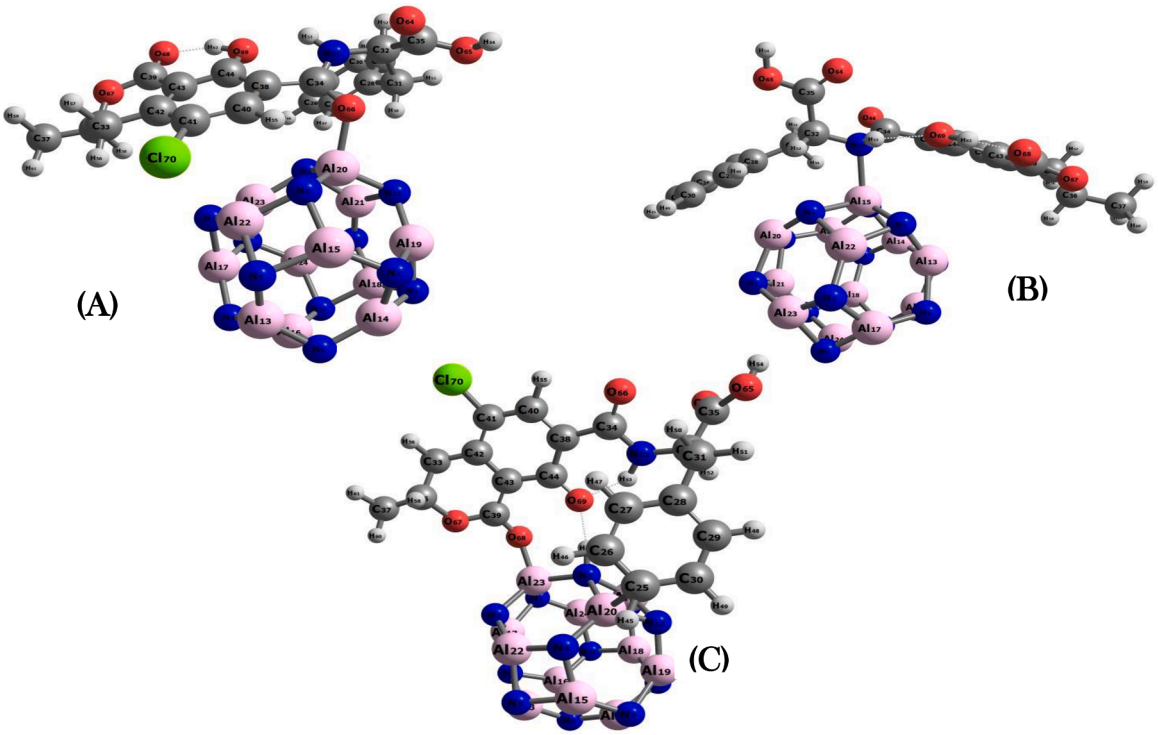

Fig. 2. Optimized structure of the studied systems at DFT/PBE0/ aug-cc-pvdz basis set: Respectively, (A) represents the optimized structure of AlN-OCHRA@N interaction system, (B) represents the optimized structure of AlN-OCHRA@O interaction system, and (C) represents the optimized structure of AlN-OCHRA@Cl interaction system.

HOMO and LUMO was captured and depicted in Fig. 3 for a clearer view of the individual participating molecular orbitals as well as electronic transitions between the studied adsorbed compounds. Thus, it is obvious that the adsorption of ochra gas is more favorable and stable at the oxygen site of ochra than at the chlorine and nitrogen sites, respectively.

3.5. Natural bond orbitals analysis

Natural bond orbital analysis is an important method that provides useful insights into understanding intermolecular and intramolecular bonding. It has also proven to be an efficient tool for interpreting charge transfer and hyperconjugative interactions in a molecular system. The stabilization of the molecular system arises from the donor-acceptor interaction, referred to as the delocalization of electron density between the occupied Lewis type (bond or lone pair) and the formally unoccupied (antibonding or Rydberg) non-Lewis orbitals [60]. Herein, the second-order perturbation energy E2 value of the Fork Matrix is considered, which corresponds to the interaction (donor-acceptor) stabilization energy, a basis for understanding the strength of the interactions. Furthermore, a larger E2 value indicates a more intense and higher donating ability from the donor to the acceptor, which in turn leads to a greater extent of conjugation of the whole system. The stabilization energy associated with the delocalization of electrons between filled (i) and vacant (j) was computed using the PBEPBE/aug-cc-pvdz level of theory to elucidate the inter- and intramolecular hybridization and the delocalization of electron density within the system.

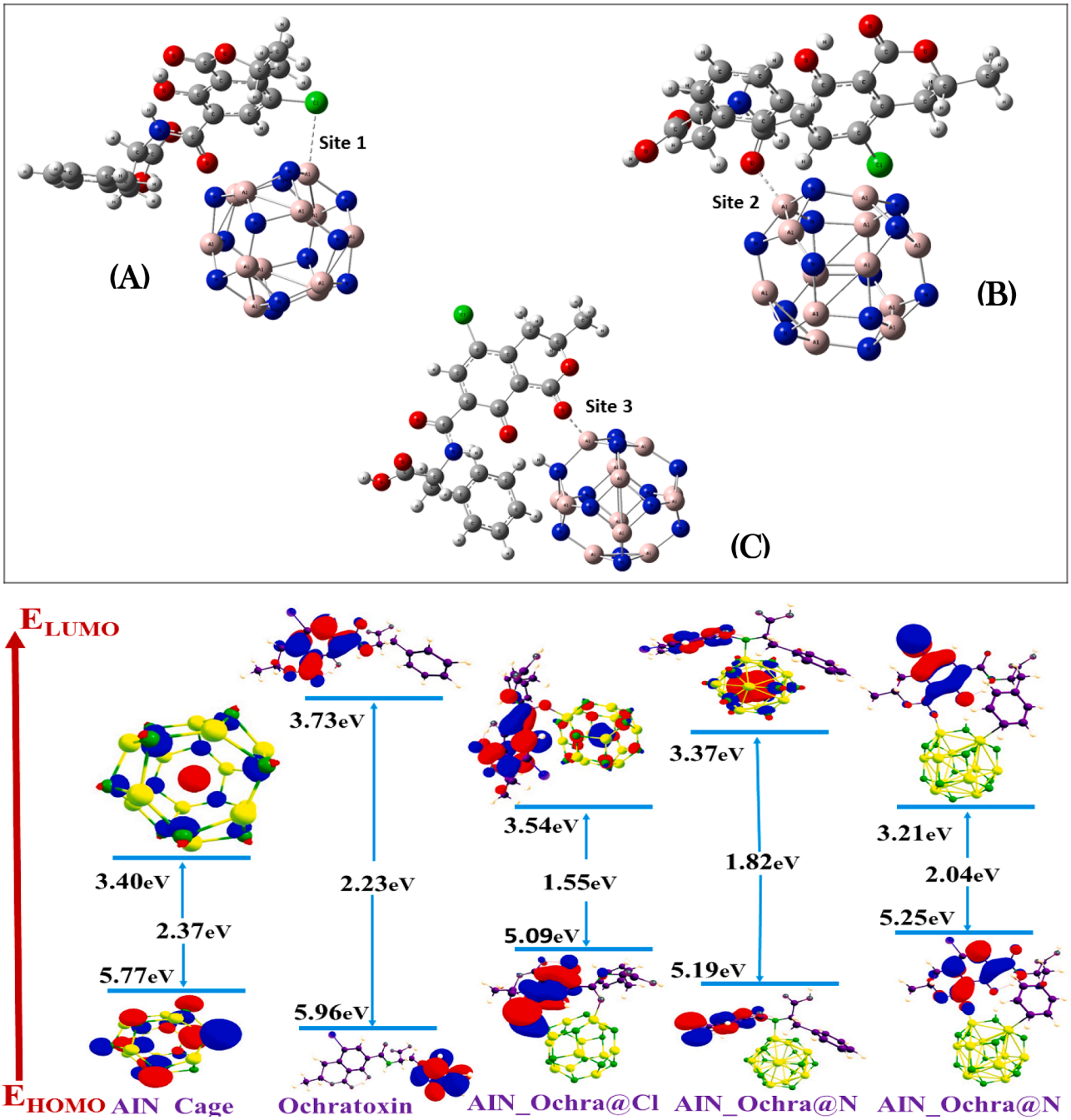

Fig. 3. Exploring Ochratoxin Adsorption on Aluminum Nitride Nanocage: Visualization of Diverse Adsorption Sites: Respectively, (A) represents the optimized structure of AlN-OCHRA@Cl system, (B) represents the optimized structure of AlN-OCHRA@O system, and (C) represents the optimized structure of AlN-OCHRA@N system. Visualization of the HOMO-LUMO isosurface for the studied systems including the IP, EA and energy gap values.

From the results shown in Table 3, it is observed that the second-order perturbation energy in AlN (cage) shows one major transition (σ→σ*) between σ N12 – Al21 → σ* N12 – Al19, σ N12 – Al20 → σ* N12 – Al19, σ N9 – Al4 →* N12 – Al19, having energies of 5.55 kcal/mol, 5.54 kcal/mol, 5.33 kcal/mol, respectively, indicating stabilization by σ→σ* transition within the nanocage. The molecule (ochratoxin), comprising three major transitions, reveals energies at 1298.33 kcal/mol, 668.44 kcal/mol, 536.18 kcal/mol, 280.40 kcal/mol, 271.17 kcal/mol, between πC17 – C18 → πC19 – C20, σ C16 – C17 → πC17 – C18, πC19 – C20 → σC18 – C19, σ C17 – C18 → πC19 – C20, πC14 – C16 → πC10 – O42 interactions, respectively, showing the highest donating ability by π→π as a result of its highest E2 value. Upon adsorption at different points, a difference in the transition of atoms was observed. Adsorption of the molecule on the nanocage at chlorine (Ochra@AlN..Cl) gives one major σ→σ* transition, giving values of 5829.64 kcal/mol, 15.29 kcal/mol, 12.68 kcal/mol, 8.19 kcal/mol. At nitrogen, it reveals lone pair transitions with energies of 144.42 kcal/mol, 120.84 kcal/mol, 87.12 kcal/mol, 63.34 kcal/mol, and 56.86 kcal/mol. Also, adsorption at oxygen gives similar transitions as nitrogen with lesser energies of 12.50 kcal/mol, 10.55 kcal/mol, 8.54 kcal/mol, 8.49 kcal/mol, 7.14 kcal/mol. From all observations of the different adsorption points of the molecule, Ochra@AlN..Oxygen gives the highest energy, indicating an intensive molecular interaction, electron delocalization, and a high level of conjugation among the studied adsorption points.

3.6. Mulliken & Natural Population analysis

The natural population analysis of the charges present in this study has been calculated using the Mulliken population analysis [61] and the DFT/PBE0/aug-cc-pvdz method. The investigation of atomic charges was performed because it affects the dipole moment, polarizability, electronic structure, and other molecular properties of the system [62]. The Mulliken atomic charge can describe how charges are distributed among the various sub-shells of the molecular orbitals. The charges obtained in this study are presented in Table S3 of the supporting information. The results indicate that the sum of Mulliken charges for the nitrogen interaction ranges from -2.72691 to 4.182332 a.u. For the Chlorine interaction, the sum of Mulliken charges ranges from -1.330065 to 2.546474 a.u. Finally, for the Oxygen interaction, the Mulliken charges range from -0.794900 to 1.947370 a.u. The target atom of the chlorine interaction, Cl, has a charge of 0.01005 a.u. The nitrogen interaction shows that all the nitrogen atoms had negative atomic charge values, except one with a charge value of 3.505274 a.u. All the oxygen atoms are observed to have negative atomic charges, with -0.581467 a.u. as the highest negative atomic charge. Fig. 4 depicts the visualization of the Mulliken and natural population charges. It can be deduced that the positively charged centers in each interaction are the most susceptible sites for electron donation, i.e., nucleophilic attacks. However, the trend of results indicates that the most negatively charged centers are the most susceptible sites for the electrophilic ones.

3.7. Visual study of weak interactions

3.7.1. QTAIM analysis

It is a known fact that atoms are characterized by different sets of attributes, varying between relatively small gaps [63]. Hence, not only structural investigations but also microelectronic investigations may be biased in gaining complete insights into intra and inter-molecular interactions of a given system. The Atoms in Molecule (AIM) hypothesis enables scientists to explore and gain insights into the various interactions in molecular structures by utilizing the Bond Critical Points (BCPs) [64]. The BCPs are points where the first derivative of the density of all electrons dematerializes [65]. The bond critical point is normally denoted at the bond path by a dot irrespective of the nature of the bond.

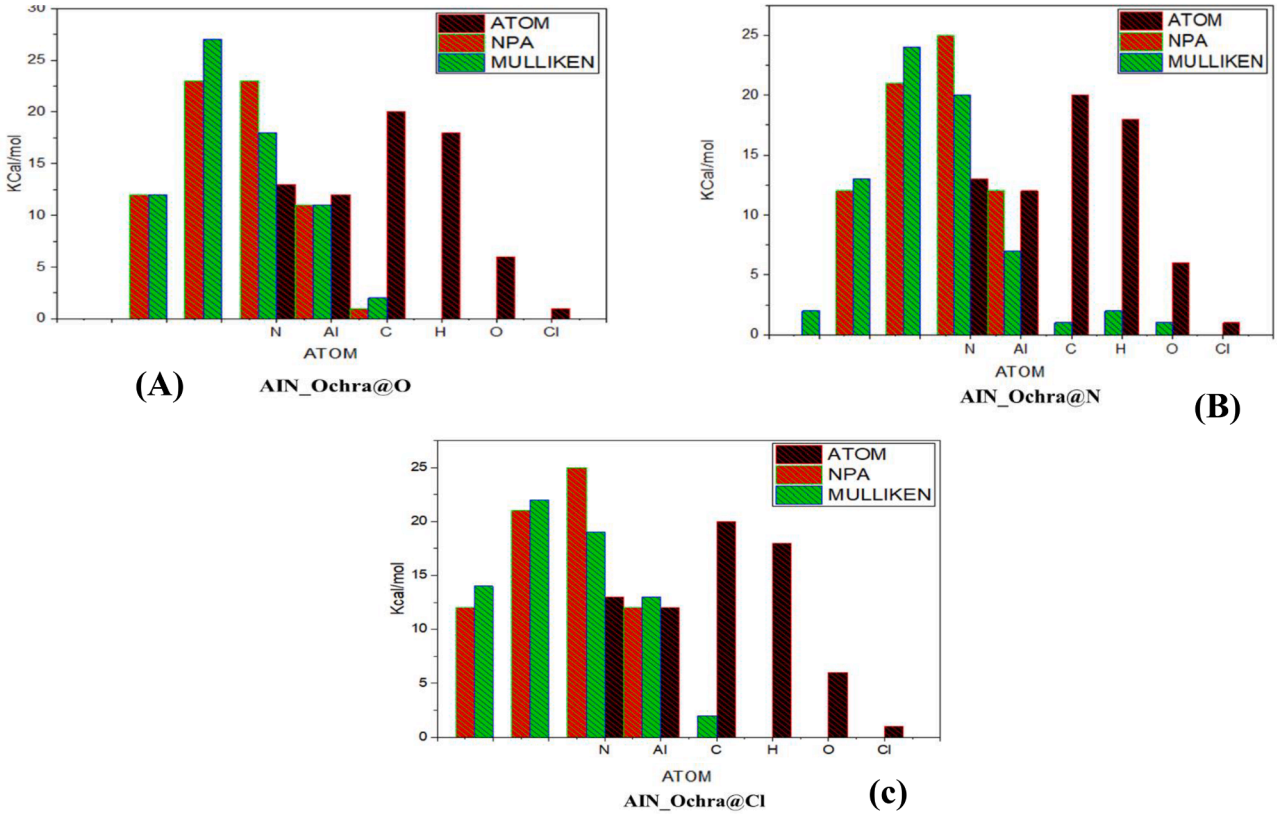

Fig. 4. Graphical representation of the Mulliken & Natural Population analysis for the studied systems: Respectively, (A) represents the Mulliken & Natural Population analysis of AlN-OCHRA@O, (B) represents the Mulliken & Natural Population analysis of AlN-OCHRA@N, and (C) represents the Mulliken & Natural Population analysis of AlN-OCHRA@Cl.

These points can be situated at the middle of different interconnecting bonds, forming a kind of ring shape called Ring Critical Point (Rcp), liaising two adjoining atoms [66]. AIM methodology is one of the most valuable and useful approaches to gaining complete insights into non-hydrogen and hydrogen bonding interactions [67]. Topological parameters have been used to classify and arrive at various conclusions in the Quantum Theory of Atoms in Molecule (QTAIM). The topological parameters, such as electronic charge density V(r), energy density H(r), Hamiltonian kinetic energy K(r), density of all electrons ρ(r), Laplacian of electron density $\nabla 2\rho(r)$, Lagrangian kinetic energy G(r), electron localization function (ELF), have been computed and presented in Table 4. Also, -G(r)/V(r) has been calculated for all studied systems at BCPs to gain more insights into the covalent, partial covalent, and non-covalent nature of interactions. As such, the results obtained are carefully presented in Table 4. Classification into covalent, partial covalent, and non-covalent can be achieved by simultaneously considering the directions of charge density ρ(r) as well as electron density $\nabla 2\rho(r)$ of the interaction. As such, when $\nabla 2\rho(r) > 0$ and $H(r) > 0$, it depicts a non-covalent interaction. However, partial covalent interaction is easily pinpointed when $\nabla 2\rho(r) > 0$ and $H(r) < 0$. It is observed that an interaction is categorized as non-covalent interaction when $\nabla 2\rho(r) < 0$ and $H(r) < 0$, respectively. The results in Table 4 explained that the positive directions of the charge density ρ(r) and electron density resulting in $\nabla 2\rho(r) > 0$ and $H(r) > 0$ suggest the presence of non-covalent interaction between all the studied compounds. The binding energy between each critical point of interaction for ochratoxin@AlN...Chlorine, ochratoxin@AlN...Nitrogen, and ochratoxin@AlN...oxygen studied compounds elucidates that the interaction process of ochratoxin with Al12N12 nanocluster at chlorine, nitrogen, and oxygen sites were very stable. As such, the highest binding energy of −166.19 and −108.57 kcal/mol was observed at H51–N2 and O69–N5 bond critical points for ochratoxin@AlN...Nitrogen molecule. Perusing the interaction process, it was observed that the most effective intermolecular interaction occurred at N_2-H_{62}…O_{69} BCP with a binding energy of −61.72 kcal/mol for ochratoxin@AlN...oxygen compound suggesting that the surface interacted more favorably and stably at the oxygen site than at the nitrogen and chlorine site with low binding energy of −33.29 and −34.95 kcal/mol at Ochra@AlN...N and Ochra@AlN...Cl molecules respectively which contributed chiefly to the outstanding stability of Ochra@AlN...O compound. Thus the adsorption via the oxygen site is comparably preferable owing to the excellent hydrogen bonding intermolecular interaction exhibited by the said system as well as excellent energy gap and adsorption energy as reported earlier from previous electronic studies.

3.7.2. Reduced density gradient (RDG)

The reduced density gradient, commonly referred to as non-convalent interaction, provides well detail explanations on weak intermolecular interaction between two or more interacting molecules [57]. Electrostatic contacts, pi (π) effect, van der Waals forces, and the hydrophobic effect all serve as strong cues that there are multiple dimensions involved in the study of weak interactions [68]. An isosurface with colored infill elucidates more on these aforementioned types of interaction [69]. The deep blue color indicates the presence of a strong force of attraction, whereas the green isosurface indicates the presence of van der Waals force of interaction and low electron density [70]. By utilizing the RDG and the sign$\lambda 2(r)$ $\rho(r) < 0$, NCI analysis can be used to visualize the region and the type of weak interactions [71]. The sign$\lambda 2$ (r) $\rho(r) < 0$ contains the points that signify strong interaction while I n the ssign$\lambda 2(r)$ $\rho(r) \approx 0$ region, weak van der Waals interactions are detected. Conversely, if the points in sign$\lambda 2(r)$ $\rho(r) > 0$, it is likely that the interactions are repulsive and as such it often fraternized with a red isosurface map [72]. The sort, potency, and area of an interaction can also be determined by combining the electron density ρ(r) and the second eigenvalue of the electron density Hessian matrix ($\lambda 2$) as calculated using Eq. (8) in the methodology section. When scrutinizing these interactions, it is paramount to take into consideration that the deep blue iso-surface of the investigated interactions (Ochra@AlN...Cl, Ochra@AlN...O, and Ochra@AlN...N) suggests the presence of a strong force of attraction, which is identified presence by the hydrogen bond interaction. Thus, the depth of the blue color confined by the RDG iso-surfaces and the respective spike peaks of the three interactions, which vary from −0.02 to −0.05, are remarkably similar. However, it is thought that the aforementioned interactions may experience a very weak van der Waals contact. Ochra@AlN...O evenly, on the other hand, was observed to exhibit a weaker form of interaction. But it must be demonstrated that the van der Waals interactions and attraction between the three interactions are considerably lower than those discovered inside the enclosed surfaces. This results from the spatial arrangement of the atoms, which raises the energy in the surfaces. However, the existence of nonbonding interactions does affect the shape and reactivity of ions. As such, the presence of scant van der Waals contact indicates a loss of equilibrium with a corresponding increase in the adsorption energy between the studied molecules. The green color of the 3D RDG maps, however, shows that almost all interactions have little intermolecular interactions. Visualization for the Non-Covalent Interaction of Ochra on AlN surface at Cl, N, and O interaction sites are clearly delineated in Fig. 6.

3.8. Density of states (DOS)

The density of state of a molecule, explicates the exact proportion of states that are yet to be occupied by the studied complex at each energy intervals. An isolated system such as molecules in gas or solvent phase is observed to possess different distribution of electronic densities like the spectra density. Density of state is essential for determining the carrier's concentration as well as energy distribution or contribution of each fragment to the stability of the studied adsorbed compounds. Thus, DOS is represented as a distribution by a probability density function as such is the average over the space and time domains of the various states occupied by the compounds of interest. Per se, all information related to the dispersion relations of the various properties of a system is well explicated at the DOS plot [73]. However, the properties of each orbitals at each energy range is clearly shown in Fig. 7 The total density of state (TDOS) map, partial density of state, as well as the overlap partial density of state (OPDOS) of aluminum nitride nanocluster interaction with ochra at oxygen, nitrogen and chlorine sites (ochra@$Al_{12}N_{12}$....O, ochra@$Al_{12}N_{12}$.....N, ochra@$Al_{12}N_{12}$....Cl) were plotted using Multiwfn and origin software's as shown below (see Fig. 7). The obtained result suggests that ochra fragment gave the highest contribution at the highest occupied molecular orbital (HOMO) level from −0.4 to −0.7ev for ochra@$Al_{12}N_{12}$...O system which is observed to differ at ochra@$Al_{12}N_{12}$...N and ochra@$Al_{12}N_{12}$...Cl compounds where ochra fragment only dominated from −0.5 to −0.6ev. Whereas the highest contribution observed from −0.5 to −0.3ev at the HOMO region was dominated by $Al_{12}N_{12}$ fragment for ochra@$Al_{12}N_{12}$...Cl and ochra@$Al_{12}N_{12}$...N molecules respectively. Ochra fragment was seen to also dominate at the lowest unoccupied molecular orbital for ochra@$Al_{12}N_{12}$...O compound which is in tandem with the energy gap (Eg) of 2.04Ev from Table 4, depicting that ochra fragment played a key role in stabilizing the said molecule which is not the case for other systems with a corresponding low Eg of 1.55 and 1.82ev for ochra@$Al_{12}N_{12}$...Cl and ochra@$Al_{12}N_{12}$....N compounds respectively. Similar trend was observed at the LUMO region for ochra@$Al_{12}N_{12}$...Cl and ochra@$Al_{12}N_{12}$....N system, where $Al_{12}N_{12}$ fragment contributed more to the stability of both compounds from −0.2 to 0.2ev respectively. Hence, the slight shift at the LUMO region from ochra@$Al_{12}N_{12}$...Cl to ochra@$Al_{12}N_{12}$....O is responsible for the molecular stabilization of the studied nanoclusters.

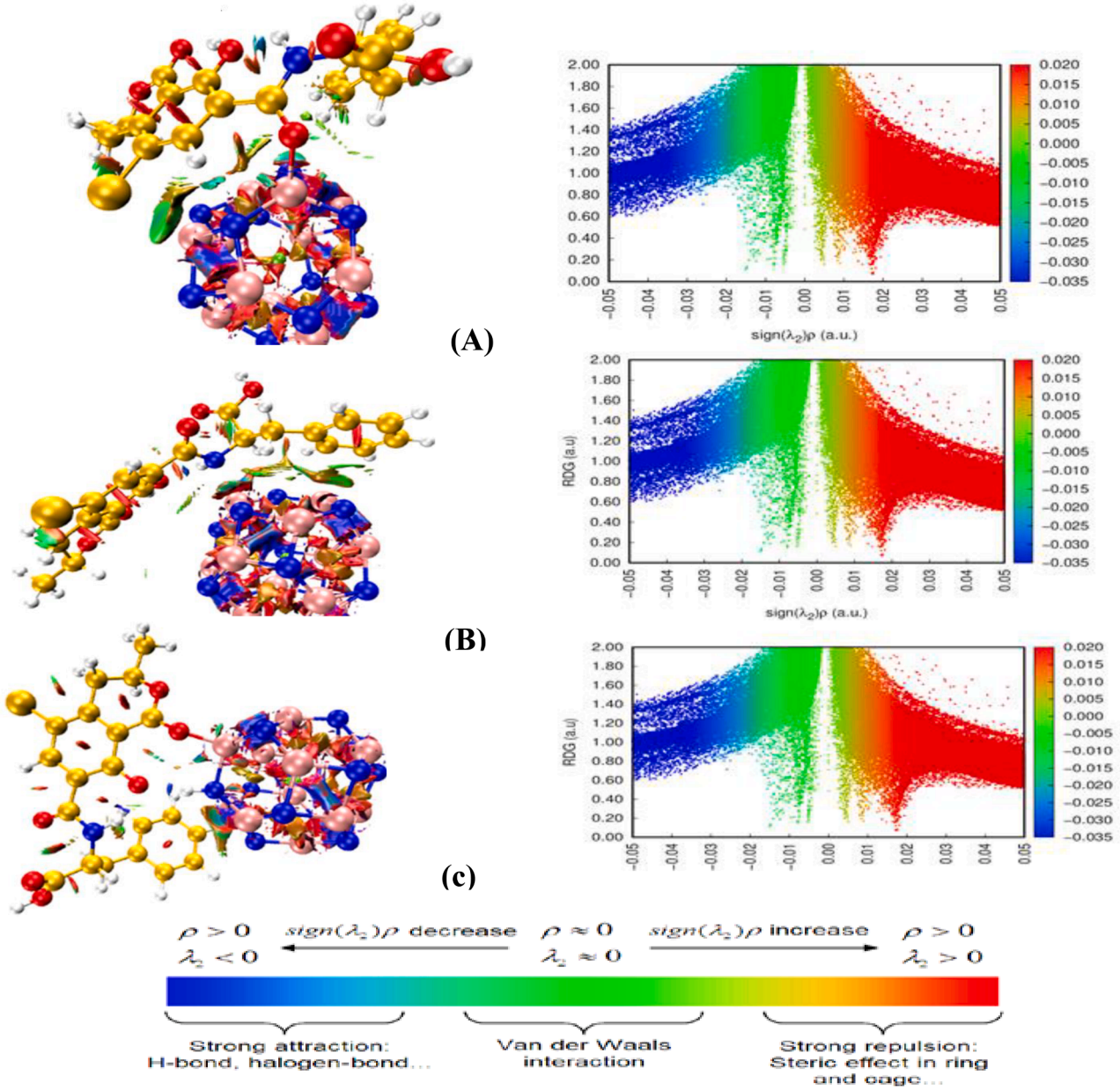

Fig. 6. Graphical representation of non-covalent interaction of Ochra on $Al_{12}N_{12}$ surface at Cl, N and O sites respectively. Note: (A) represents the non-covalent interactions of AlN-OCHRA@O system, (B) represents the non-covalent interactions of AlN-OCHRA@N system, and (C) represents the non-covalent interactions of AlN-OCHRA@Cl system.

3.9. Sensor mechanism

The mechanisms of sensing represent those parameters that characterized the potency and performance of sensor devices. Many parameters such as fraction of electron transfer, chemical conductivity, energy gap, work function (φ), Fermi energy level, recovery and response time have been selected based on their ability to validate the performance any sensing system. In this present study, the sensing performances of the studied systems are presented in Table 5:

3.9.1. Electrical conductivity

The ability and capability to move electron from valence band to conduction band can be related with electrical conductivity of that studied system [74,75]. Furthermore, the electrical conductivity is dependent on the movement of electron from the combining power (valence) to the conduction band. The Mathematical expression showing the relationship between the electrical conductivity and adsorption energy are given in Eq. (8). Since the relationship is inverse, it indicates that the difference in electronic properties of Ochra@AlN...Chlorine, Ochra@AlN...Nitrogen and Ochra@AlN...Oxygen can direct effect changes in resistivity and indirect in the electrical conductivity.

$$\boldsymbol{\sigma} = \boldsymbol{AT}^{2/3}\boldsymbol{e}^{\left(E_g/2KT\right)} \tag{8}$$

where σ, A, K and T denote the electrical conductivity, constant, Boltzmann constant and temperature respectively. To compute the sensing response, Eq. (9) is applied and related with resistivity.

$$\boldsymbol{S} = \frac{|\boldsymbol{R}_2 - \boldsymbol{R}_1|}{\boldsymbol{R}_1} = \left|\frac{\boldsymbol{R}_2}{\boldsymbol{R}_1}\right| - 1 \tag{9}$$

Where the resistivity of the adsorbent and the adsorbate is denoted by R_1 and R_2 respectively. From the inverse relationship between resistivity and conductivity, it can be deduced that the system with greater

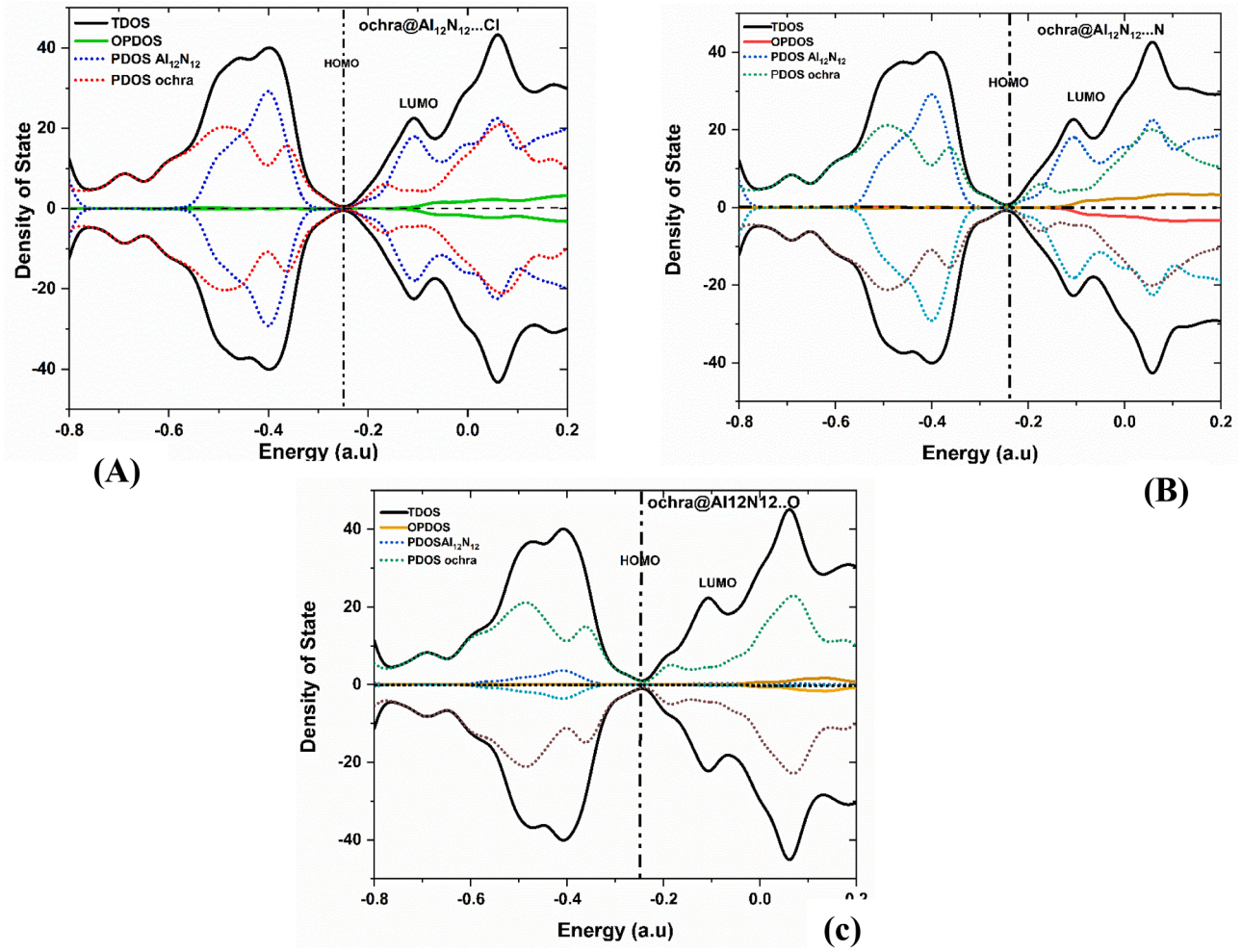

Fig. 7. Graphical representation of the Density of states (DOS) for the studied interaction: (A) represents the non-covalent interactions of AlN-OCHRA@Cl system, (B) represents the non-covalent interactions of AlN-OCHRA@N system, and (C) represents the non-covalent interactions of AlN-OCHRA@O system.

adsorption or interaction energy often accompany low resistivity [71, 72].

$$S = \left|\frac{\sigma_2}{\sigma_1}\right| - 1 = e^{(|E_g|/2KT)} \tag{10}$$

The electrical conductivities of the surfaces and studied systems are designated by σ1 and σ2 from the Eq. (10). The key factors in Eq. (10) is the band gap (E_g). This indicates that the greater the band gap, the lesser the conductivity of a material. One can observe from Table 2 of the FMO analysis section that: AlN and Ochra with energy gaps of 2.37 eV and 2.8923 eV respectively has relatively greater resistivity. Whereas, the least resistivity is found in the Ochra@AlN...Chlorine system of energy gap value 1.5538 eV. Other lower resistivity is observed in Ochra@AlN...Oxygen and Ochra@AlN...Nitrogen systems with energy gap values of 1.7987 eV and 2.0436 eV respectively. To conclude from Table 5, that, Ochra@AlN...Chlorine with the least resistivity (greater conductivity) possess better sensing attribute than its studied counterparts at room temperature of 300 K. From Fig. 8, as the temperature of the system increases above room 300 K, the electrical conductivity increases from 1000 K for all the interaction but this is more significant for Ochra@AlN...O followed by Ochra@AlN...N and least for Ochra@AlN...Cl

3.9.2. Recovery and response time

As one of the essential parameters in sensor designs, the interaction strength of an adsorption process can be determined by the recovery time. The sensing response time of a sensor is directly related to the adsorption energy and gives information on how fast a surface can respond on interacting with the absorbate in this case the ochratoxin and produce electrical signal that can be measured by appropriate electronic device. The Mathematical relation between the adsorption energy and recovery (τ) and response time (S) are depicted in Eqs. (11) and (12) as:

$$\tau = V_0^{-1} e^{-E_{ad}/KT} \tag{11}$$

Table 2
FMO table for the studied compound calculated at DFT/PBE0/ aug-cc-pvdz method.

Systems	HOMO(eV)	LUMO(eV)	IP(eV)	EA(eV)	μ(eV)	X(eV)	Ƞ(eV)	Eg(eV)	σ(eV)	ω(eV)
Ochratoxin	−5.99	−3.81	5.96	3.73	−4.84	4.84	1.12	2.23	0.89	13.09
AIN_CAGE	−5.71	−3.27	5.77	3.40	−4.59	4.59	1.19	2.37	0.84	12.44
Ochra@AlN..Cl	−5.17	−3.54	5.09	3.54	−4.31	4.31	0.78	1.55	1.28	7.21
Ochra@AlN..N	−5.17	−3.27	5.19	3.37	−4.29	4.29	0.91	1.82	1.09	8.37
Ochra@AlN..O	−5.17	−3.27	5.25	3.21	−4.23	4.23	1.02	2.04	0.98	9.14

Table 3
Natural orbital table for the studied nanocage and interaction calculated at DFT/ PBE0/ aug-cc-pvdz method.

Transitions	Donor(i)	Acceptor(j)	E^2 Kcal/ mol	E(j)-E(i) a.u	F(i,j) a. u
AlN	σ N_{12} – Al_{21}	σ * N_{12} – Al_{19}	5.55	0.59	0.051
	σ N_1 – Al_{17}	σ * N_1 – Al_{24}	5.55	0.59	0.051
	σ N_{12} – Al_{20}	σ * N_{12} – Al_{19}	5.54	0.59	0.051
	σ N_9 – Al_{14}	σ * N_{12} – Al_{19}	5.33	0.59	0.050
	σ N_{12} – Al_{20}	σ * N_{11} – Al_{21}	5.32	0.59	0.050
Ochra	π *C_{17} – C_{18}	π *C_{19} – C_{20}	1298.33	0.95	1.525
	σ C_{16} – C_{17}	π *C_{17} – C_{18}	668.44	1.19	0.885
	π *C_{19} – C_{20}	σ *C_{18} – C_{19}	536.18	0.29	0.718
	σ C_{17} – C_{18}	π *C_{19} – C_{20}	280.40	2.15	0.779
	π *C_{14} – C_{16}	π *C_{10} – O_{42}	271.17	0.01	0.087
Ochra@AlN.. Cl	σ N_1 – Al_{24}	σ * N_2 – Al_{21}	5829.64	0.08	0.602
	σ N_1 – Al_{23}	σ * N_7 – Al_{14}	15.29	0.35	0.066
	σ N_1 – Al_{23}	σ * N_7 – Al_{19}	12.68	0.29	0.055
	σ N_1 – Al_{21}	σ * N_1 – Al_{24}	8.19	0.51	0.058
Ochra@AlN.. N	Lp $_{(1)}$ N_3	Lp*$_{(1)}$ Al_{21}	144.42	0.50	0.234
	σ N_5 – Al_{13}	Lp*$_{(1)}$ Al_{21}	120.84	0.18	0.136
	Lp* $_{(1)}$ Al_{14}	Lp*$_{(1)}$ Al_{15}	87.12	0.01	0.059
	Lp* $_{(2)}$ Al_{14}	Lp*$_{(1)}$ Al_{21}	63.34	0.15	0.088
	$Lp_{(1)}$ N_3	σ*N_{10} – Al_{16}	56.86	0.72	0.184
Ochra@AlN.. O	Lp $_{(1)}$ N_2	Lp*Al_{23}	12.50	0.35	0.060
	Lp $_{(1)}$ N_2	σ* N_2 – Al_{23}	10.55	0.47	0.064
	σN_2 – Al_{23}	Lp* Al_{20}	8.54	0.41	0.055
	σN_2 – Al_{23}	Lp* Al_{21}	8.49	0.42	0.055
	σN_3 – Al_{23}	Lp* Al_{17}	7.14	0.41	0.050

Table 5
Electrical conductivity, Response time and Recover time of Different interaction of the Ochratoxin with AlN surface at room temperature 300 K.

	Electrical conductivity (S/m)	Response time (s)	Recovery time (s)
Ochra@AlN... Cl	5.6E 4	1.616	1.6E-156
Ochra@AlN... N	5.2E 4	1.757	1.94E-86
Ochra@AlN... O	4.8E 4	1.881	3.3E-158

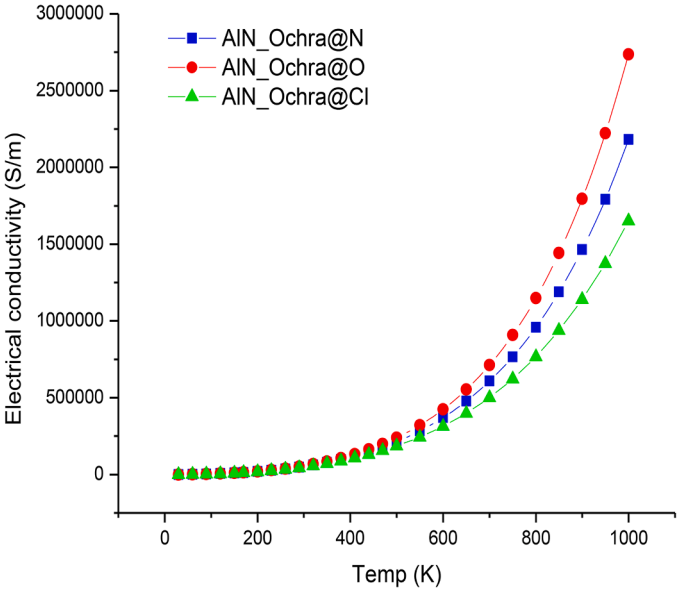

Fig. 8. Plot illustrating the effect of Temperature on the Electrical Conductivity on Ochra@AlN system.

Table 4
Values of the topological parameters of the BCPs of Ocha@AlN...Oxygen, Ocha@AlN...Nitrogen, Ocha@AlN...chlorine interaction obtained from the QTAIM analysis.

Interaction	Bond	BCP	ρ(r)	$\nabla^2\rho(r)$	G(r)	K(r)	V(r)	H(r)	G(r)/ V	(E.P) S	ELF	ALIE	$\Psi_{orbital}$	RDG
ochra@AlN...Cl	Al22 – Cl70	173	0.16	0.25	0.79	0.17	−0.97	−0.17	0.82	0.54	0.11	0.58	−0.36	0.55
	$BE(E_{Al—Cl})$	−34.95 kcal/mol												
	H47 – N2	105	0.11	0.34	0.69	−0.16	−0.54	0.16	1.29	0.05	0.48	0.50	0.60	0.55
	$BE(E_{H—N})$	−23.75 kcal/mol												
	N4 – H55	148	0.18	0.65	0.14	−0.27	−0.11	0.26	1.24	0.16	0.63	0.54	−0.43	0.16
	$BE(E_{K—N})$	−39.32 kcal/mol												
Ocha@AlN...N	N4 – N63	161	0.15	0.53	0.11	−0.20	−0.91	0.20	0.12	0.37	0.55	0.53	0.97	0.49
	$BE(E_{N—N})$	−33.29 kcal/mol												
	N4 – C29	157	0.15	0.27	0.74	0.66	−0.80	−0.66	0.92	1.93	0.10	0.53	0.11	0.51
	$BE(E_{N—C})$	−31.78 kcal/mol												
	H51 – N2	151	0.75	0.22	0.46	−0.99	−0.36	0.99	1.28	0.66	0.31	0.52	−0.43	0.33
	$BE(E_{H—N})$	−166.19 kcal/ mol												
	O69 – N5	139	0.49	0.17	0.37	−0.63	−0.30	0.63	1.2	0.09	0.12	0.49	0.31	0.56
	$BE(E_{H—N})$	−108.57 kcal/ mol												
Ocha@AlN...O	Al20 – C25	104	0.22	0.68	0.18	0.88	−0.19	−0.88	0.95	0.25	0.69	0.83	−0.1026	0.31
	$BE(E_{Al—C})$	−48.33 kcal/mol												
	N2 – H62 … O69	119	0.28	0.11	0.25	−0.18	−0.23	0.18	1.08	0.02	0.84	0.59	−0.11	0.52
	$BE(E_{N—H…O})$	−61.72 kcal/mol												

$$S = e^{(|\Delta E_g|/2KT)-1} \quad (12)$$

Where K designates the Boltzmann constant which approximately equals to. $\sim 2.0 \times 10^{-3}$ kcal/mol., V_0 is the attempt frequency equivalent to 10^12 for a first order interaction and T is the temperature, Table 1 of the adsorption study shows that Ochra@AlN-N interaction is with the least negative adsorption energy of −0.7730 eV and thus, possess fastest recovery time of 1.94E-86 s, followed by 1.6E-156 s for Cl and the least being 3.3E-158 s for Ochra@AlN-O. Fig. 9(a) indicates the effect of temperature on the recovery time of different spatial interaction of Ochratoxin on AlN surface. As the temperature increase, the recovery time for all the interactions fluctuates around the same mean value except for Ochra@AlN...N with much faster recovery time below room temperature. Similarly, from Fig. 9(b), the response time indicates decreased as the adsorption energy increase. The spatial orientation of Ochra@AlN...Cl indicates to have the fastest response with a time of 1.616 s, followed by 1.757 s for Ochra@AlN...N and the least responsive being 1.881 s for Ochra@AlN...Cl. in the same order, increase in temperature increases the response time which is more significant for Ochra@AlN...O, Ochra@AlN...N and Ochra@AlN...Cl as the most responsive.

4. Conclusions

The PBE0 functional has been utilized using the aug-cc-pvdz basis set to study the adsorption behavior of the interaction named Ochra@AlN, Ochra@AlN..N and Ochra@AlN..O, respectively, on the AlN nanocage. Notable observations from the study reveal that the Ochra@AlN..N interaction has shorter bond distances than Ochra@AlN..O and Ochra@AlN..Cl, making it more stable compared to the other studied interactions. The adsorption study reveals that the Ochra@AlN..O interaction obtained a higher adsorption energy and exhibits better sensing performance than Ochra@AlN..N and Ochra@AlN..Cl, respectively. Investigation of the electronic properties shows that Ochra@AlN..O, with an energy gap value of 2.04 eV, possesses a higher energy gap after doping, making it the most stable among the compounds. The natural bond orbitals reveal that Ochra@AlN..O gives the highest second-order perturbation energy and high electron delocalization with a high level of conjugation among the studied interactions. The electrical conductivity showed that Ochra@AlN..Cl obtained the least resistivity (greater conductivity) and possesses better sensing attributes than its studied counterparts, followed by Ochra@AlN..O and Ochra@AlN..N, respectively. The investigation of the recovery time showed that the Ochra@AlN..O system has the greatest negative adsorption energy of −2.466 eV and thus possesses a higher recovery time, and temperature changes above room temperature have no effect. From all indications, it can be concluded that the adsorption of the Ochratoxin gas on the aluminum nitride is strong in all the studied gases, with Ochra@AlN..O possessing a higher sensing attribute than its studied counterparts.

Ethics approval and consent to participate

Not applicable

Consent for publication

Not applicable

Availability of data and material

All data are contained within the manuscript and manuscript supporting information document (ESI).

Competing interests

The authors declare no form of any conflict of ineterest.

Author contributions

Ernest C. Agwamba: Conceptualization, design, analysis, writing, and editing. Hitler Louis: Project administration, supervision, validation, writing, and analysis. Innocent Benjamin: Editing, graphics, writing, result analysis, manuscript final draft. Gideon E. Mathias: Results analysis, writing, editing, and manuscript first draft. Ernest E. Ekereke and Eze F. Ahuekwe: Analysis, writing and manuscript final draft.: Adeyinka S. Adeyemi: Resources and Methodology,

Funding

No funding was received from any Government or Non-Government organization.

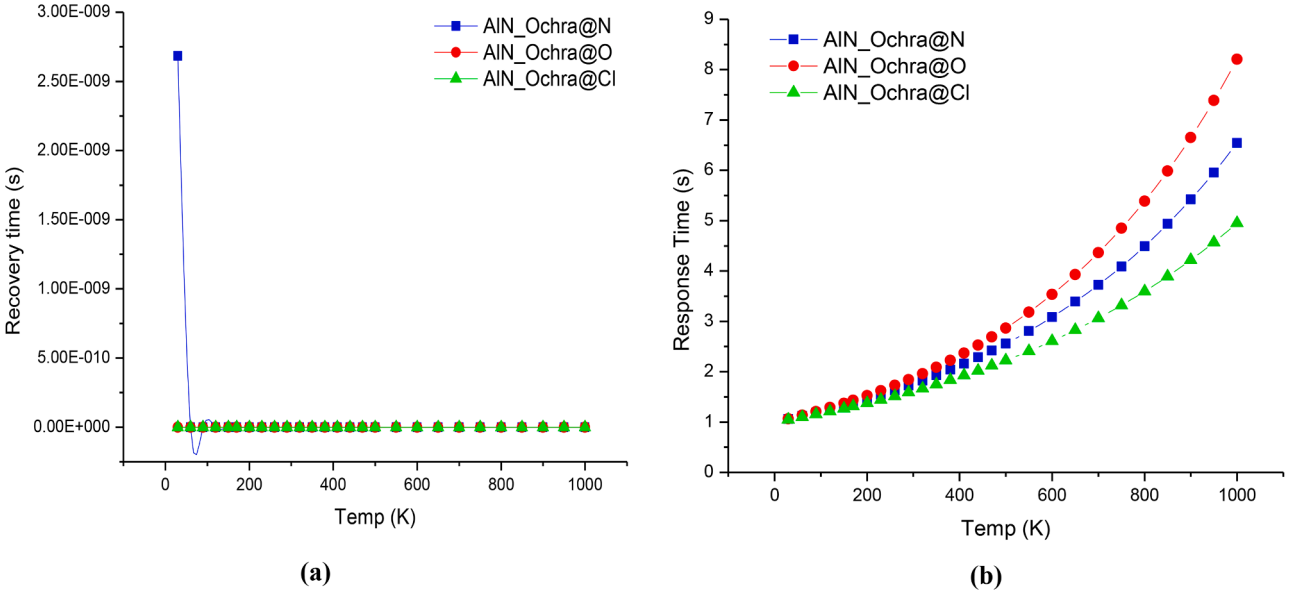

Fig. 9. Plots illustrating the effect of Temperature on the (a) Recovery and (b)Response time of Ochra@AlN interactions.

Declaration of Competing Interest

The authors declare that they have no known competing financial interests or personal relationships that could have appeared to influence the work reported in this paper.

Data availability

Data will be made available on request.

Acknowledgments

The center for high performance computing (CHPC) South Africa is acknowledged for providing the computational resources utilized in this work.

Supplementary materials

Supplementary material associated with this article can be found, in the online version, at doi:10.1016/j.chphi.2023.100221.

References

[1] Z. Naeem, K. Jabeen, S. Iqbal, Management of ochratoxigenic fungi by phytochemicals of amaranthus viridis l, J. Anim. Plant Sci. 32 (4) (2022) 1136–1142.
[2] G.S. Shephard, Determination of mycotoxins in human foods, Chem. Soc. Rev. 37 (11) (2008) 2468–2477.
[3] S. Tasić, N. Miladinović-Tasić, Cladosporium spp.: cause of opportunistic mycoses, Acta Fac. Med. Naissensis 24 (1) (2007) 15–19.
[4] P. Jeswal, D. Kumar, Mycobiota and natural incidence of aflatoxins, ochratoxin A, and citrinin in Indian spices confirmed by LC-MS/MS, Int. J. Microbiol. (2015). *2015*.
[5] Fapohunda, S.O. (2014). Moulds, meals, man and mycotoxins. Nigeria mycotoxin awareness and study network NMASN.
[6] United Nations Industrial Development Organization/Food and Agriculture Organization of the United Nations (UNIDO/FAO). (2006). Herbs, spices and essential oils, post-harvest operations in developing countries. Austria: UNIDO/FAO.
[7] M. Jalili, S. Jinap, Natural occurrence of aflatoxins and ochratoxin A in commercial dried chili, Food Control 24 (1–2) (2012) 160–164.
[8] G.A. Lombaert, P. Pellaers, G. Neumann, D. Kitchen, V. Huzel, R. Trelka, P. M. Scott, Ochratoxin A in dried vine fruits on the Canadian retail market, Food Addit. Contam. 21 (6) (2004) 578–585.
[9] F. Ozbey, B. Kabak, Natural co-occurrence of aflatoxins and ochratoxin A in spices, Food Control 28 (2) (2012) 354–361.
[10] P.C. Okwara, I.S. Afolabi, E.F. Ahuekwe, Application of laccase in aflatoxin B1 degradation: a review, IOP Conf. Ser. Mater. Sci. Eng. 1107 (1) (2021), 012178.
[11] M. Ardic, Y. Karakaya, M. Atasever, H. Durmaz, Determination of aflatoxin B1 levels in deep-red ground pepper (isot) using immunoaffinity column combined with ELISA, Food Chem. Toxicol. 46 (2008) 1596–1599.
[12] N. El Darra, L. Gambacorta, M. Solfrizzo, Multimycotoxins occurrence in spices and herbs commercialized in Lebanon, Food Control 95 (2019) 63–70.
[13] Tiffany, I. (2013). The implication of aflatoxin contamination for local food safety in Senegal. *Available from: www. hun gercenter. wpengine. netdna-cdn. com.*
[14] Okello, D.K., Kaaya, A.N., Bisikwa, J., Were, M., & Oloka, H.K. (2010). Management of aflatoxins in groundnuts: a manual for farmers, processors, traders and consumers in Uganda. Entebbe: National Agricultural Research Organisation, 1–38.
[15] International Agency for Research on Cancer (IARC). (1993). Some naturally occurring substances, food items and constituents, heterocyclic aromatic amines and mycotoxins. vol. 56, Lyon, France. World Health Organization. 489–521.
[16] R. Zheng, H. Xu, W. Wang, R. Zhan, W. Chen, Simultaneous determination of aflatoxin B1, B2, G1, G2, ochratoxin A, and sterigmatocystin in traditional Chinese medicines by LC–MS–MS, Anal. Bioanal. Chem. 406 (13) (2014) 3031–3039.
[17] S. Lasram, H. Hajri, Z. Hamdi, Aflatoxins and ochratoxin A in Red Chili (Capsicum) powder from Tunisia: co-occurrence and fungal associated microbiota, J. Food Qual. Hazards Control 9 (1) (2022) 32–42.
[18] Z. Zareshahrabadi, R. Bahmyari, H. Nouraei, H. Khodadadi, P. Mehryar, F. Asadian, K. Zomorodian, Detection of aflatoxin and ochratoxin A in spices by high-performance liquid chromatography, J. Food Qual. (2020) 2020.
[19] Y. Wei, P. Liu, Analysis of the nature of interaction between AlN nanocage and ibuprofen using quantum chemical study, Struct. Chem. 32 (4) (2021) 1685–1692, https://doi.org/10.1007/s11224-021-01750-w.
[20] E. Vessally, M. Vali, A. Hosseinian, M.R.P. Heravi, A. Bekhradnia, Mustard gas adsorption on the pristine and BN-doped graphynes: a computational study, Phys. Lett. A 384 (21) (2020), 126479.
[21] M. Wang, L. Yang, B. Hu, J. Liu, L. He, Q. Jia, Z. Zhang, Bimetallic NiFe oxide structures derived from hollow NiFe Prussian blue nanobox for label-free electrochemical biosensing adenosine triphosphate, Biosens. Bioelectron. 113 (2018) 16–24.
[22] V. Kumar, K. Vaid, S.A. Bansal, K.H. Kim, Nanomaterial-based immunosensors for ultrasensitive detection of pesticides/herbicides: current status and perspectives, Biosens. Bioelectron. 165 (2020), 112382.
[23] L. Zhang, Y. Ying, Y. Li, Y. Fu, Integration and synergy in protein-nanomaterial hybrids for biosensing: strategies and in-field detection applications, Biosens. Bioelectron. 154 (2020), 112036, https://doi.org/10.1016/j.bios.2020.112036. Doi:.
[24] Q. Zhao, D. Lu, G. Zhang, D. Zhang, X. Shi, Recent improvements in enzyme-linked immunosorbent assays based on nanomaterials, Talanta 223 (1) (2021), 121722, https://doi.org/10.1016/j.talanta.2020.121722. Doi:.
[25] K.R. Singh, P.R. Solanki, B.D. Malhotra, A.C. Pandey, R.P. Singh, Introduction to nanomaterials: an overview toward broad-spectrum applications, Nanomater. Bionanotechnol. (2021) 1–35, https://doi.org/10.1201/9781003139744-1.
[26] M. Usman, M. Farooq, A. Wakeel, A. Nawaz, S.A. Cheema, H. ur Rehman, M. Sanaullah, Nanotechnology in agriculture: current status, challenges and future opportunities, Sci. Total Environ. 721 (2020), 137778.
[27] X. Zhou, Y. Wang, C. Gong, B. Liu, G. Wei, Production, structural design, functional control, and broad applications of carbon nanofiber-based nanomaterials: a comprehensive review, Chem. Eng. J. 402 (2020), 126189, https://doi.org/10.1016/j.cej.2020.126189. Doi:.
[28] N.L. Hadipour, A. Ahmadi Peyghan, H. Soleymanabadi, Theoretical study on the Al-doped ZnO nanoclusters for CO chemical sensors, J. Phys. Chem. C 119 (11) (2015) 6398–6404.
[29] D. Kohl, The role of noble metals in the chemistry of solid-state gas sensors, Sens. Actuators B 1 (1–6) (1990) 158–165.
[30] N. Li, C.P. Ho, S. Zhu, Y.H. Fu, Y. Zhu, L.Y.T. Lee, Aluminium nitride integrated photonics: a review, Nanophotonics (2021), https://doi.org/10.1515/nanoph-2021-0130.
[31] İ. Muz, H. Kurban, M. Kurban, A DFT study on stability and electronic structure of AlN nanotubes, Mater. Today Commun. 26 (2021), 102118.
[32] F. Kish, V. Lal, P. Evans, S.W. Corzine, M. Ziari, T. Butrie, D. Welch, System-on-chip photonic integrated circuits, IEEE J. Sel. Top. Quantum Electron. 24 (1) (2017) 1–20.
[33] J. Riemensberger, A. Lukashchuk, M. Karpov, W. Weng, E. Lucas, J. Liu, T. J. Kippenberg, Massively parallel coherent laser ranging using a soliton microcomb, Nature 581 (7807) (2020) 164–170.
[34] Li, N., Chao, Q., Gu, Z., Song, S., Zhou, Y., Zheng, S., ... & Lee, L. (2021, March). Photonic crystal MEMS emitter for chemical gas sensing. In MOEMS and Miniaturized Systems XX (Vol. 11697, pp. 145–151). SPIE.
[35] D. Kim, M.I. Ibrahim, C. Foy, M.E. Trusheim, R. Han, D.R. Englund, A CMOS-integrated quantum sensor based on nitrogen–vacancy centres, Nat. Electron. 2 (7) (2019) 284–289.
[36] B.J. Shastri, A.N. Tait, T. Ferreira de Lima, W.H. Pernice, H. Bhaskaran, C. D. Wright, P.R. Prucnal, Photonics for artificial intelligence and neuromorphic computing, Nat. Photonics 15 (2) (2021) 102–114.
[37] A.W. Elshaari, W. Pernice, K. Srinivasan, O. Benson, V. Zwiller, Hybrid integrated quantum photonic circuits, Nat. Photonics 14 (5) (2020) 285–298.
[38] J. Zhang, Q. Kong, Z. Zhou, P. Liu, Acetaminophen drug detection by a promising sensor of aluminum nitride nanocage: DFT approach, Monatshefte Chem. Chem. Mon. 152 (5) (2021) 481–488, https://doi.org/10.1007/s00706-021-02770-2.
[39] R. Mohammadi, A. Hosseinian, E.S. Khosroshahi, L. Edjlali, E. Vessally, DFT study on the adsorption behavior and electronic response of AlN nanotube and nanocage toward toxic halothane gas, Phys. E 98 (2018) 53–59, https://doi.org/10.1016/j.physe.2017.12.019.
[40] C. Gan, P. Liu, Adsorption behavior of anticancer drug on the aluminum nitride surface: density functional theory evolution, Phosphorus Sulfur Silicon Relat. Elem. 196 (12) (2021) 1061–1070, https://doi.org/10.1080/10426507.2021.1966428.
[41] Jasim, S.A., Kzar, H.H., Jalil, A.T., Kadhim, M.M., Mahmoud, M.Z., Al-Gazally, M. E., Nasser, H.A. & Ahmadi, Z. (2022). DFT investigation of BN, AlN, and SiC fullerene sensors for arsine gas detection and removal. Main Group Chem., 21(2). 513–521. DOI: 10.3233/MGC-210145.
[42] H. Anaraki-Ardakani, A computational study on the application of AlN nanotubes in Li-ion batteries, Phys. Lett. A 381 (11) (2017) 1041–1046.
[43] A. Seif, M. Mirzaei, M. Aghaie, A. Boshra, AlN nanotubes: a DFT study of Al-27 and N-14 electric field gradient tensors, Z. Naturforsch. A 62 (12) (2007) 711–715.
[44] J. Sołtys, M. Ptasinska, J. Piechota, S. Krukowski, Density functional study of GaN (0001)/AlN (0001) high electron mobility transistor structures, J. Cryst. Growth 401 (2014) 30–32.
[45] S. Krukowski, P. Kempisty, P. Strąk, Foundations of ab initio simulations of electric charges and fields at semiconductor surfaces within slab models, J. Appl. Phys. 114 (14) (2013), 143705.
[46] S.H. Yoo, M. Todorova, D. Wickramaratne, L. Weston, C.G.V.D. Walle, J. Neugebauer, Finite-size correction for slab supercell calculations of materials with spontaneous polarization, npj Comput. Mater. 7 (1) (2021) 58.
[47] P. Kempisty, S. Krukowski, On the nature of surface states stark effect at clean GaN (0001) surface, J. Appl. Phys. 112 (11) (2012), 113704.
[48] Frisch, M.E., Trucks, G.W., Schlegel, H.B., Scuseria, G.E., Robb, M.A., Cheeseman, J.R., ... & Fox, D.J. (2016). Gaussian 16.
[49] W. Chen, S. Sun, Y. Liang, J. Song, Antioxidant property of quercetin–Cr (III) interaction: the role of Cr (III) ion, J. Mol. Struct. 918 (1–3) (2009) 194–197.
[50] Lu, T. (2014). Multiwfn. *Software manual.* Version, 3(6).

[51] E.D. Glendening, C.R. Landis, F. Weinhold, NBO 7.0: new vistas in localized and delocalized chemical bonding theory, J. Comput. Chem. 40 (25) (2019) 2234–2241.
[52] Dennington, R.D.I.I., Keith, T.A., & Millam, J.M. (2016). GaussView, version 6.0. 16. *Semichem Inc Shawnee Mission KS*.
[53] M. Singla, D. Sharma, N. Jaggi, Effect of transition metal (Cu and Pt) doping/co-doping on hydrogen gas sensing capability of graphene: a DFT study, Int J Hydrog. Energy 46 (29) (2021) 16188–16201.
[54] K. Chukwuemeka, H. Louis, I. Benjamin, P.A. Nyong, E.U. Ejiofor, E.A. Eno, A.L. E. Manicum, Therapeutic potential of B12N12-X (X= Au, Os, and Pt) nanostructured as effective fluorouracil (5Fu) drug delivery materials, ACS Appl. Bio Mater. (2023).
[55] I. Benjamin, H. Louis, G.A. Okon, S.W. Qader, L.E. Afahanam, C.F. Fidelis, A.L. E. Manicum, Transition metal-decorated B12n12–X (X= Au, Cu, Ni, Os, Pt, and Zn) nanoclusters as biosensors for carboplatin, ACS Omega (2023).
[56] J. Makhlouf, H. Louis, I. Benjamin, E. Ukwenya, A. Valkonen, W. Smirani, Single crystal investigations, spectral analysis, DFT studies, antioxidants, and molecular docking investigations of novel hexaisothiocyanato chromate complex, J. Mol. Struct. 1272 (2023), 134223.
[57] T.E. Gber, H. Louis, A.E. Owen, B.E. Etinwa, I. Benjamin, F.C. Asogwa, E.A. Eno, Heteroatoms (Si, B, N, and P) doped 2D monolayer MoS 2 for NH 3 gas detection, RSC Adv. 12 (40) (2022) 25992–26010.
[58] H. Louis, D.E. Charlie, I.O. Amodu, I. Benjamin, T.E. Gber, E.C. Agwamba, A. S. Adeyinka, Probing the reactions of thiourea (CH4N2S) with metals (X= Au, Hf, Hg, Ir, Os, W, Pt, and *Re*) anchored on fullerene surfaces (C59X), ACS Omega 7 (39) (2022) 35118–35135.
[59] B.E. Inah, H. Louis, I. Benjamin, T.O. Unimuke, A.S. Adeyinka, Computational study on the interactions of functionalized C24NC (NC= C,–OH,–NH2,–COOH, and B) with chloroethylphenylbutanoic acid, Can. J. Chem. (2022).
[60] C.G. Apebende, H. Louis, A.E. Owen, I. Benjamin, I.O. Amodu, T.E. Gber, F. C. Asogwa, Adsorption properties of metal functionalized fullerene (C59Au, C59Hf, C59Ag, and C59Ir) nanoclusters for application as a biosensor for hydroxyurea (HXU): insight from theoretical computation, Z. Phys. Chem. 236 (11–12) (2022) 1515–1546.
[61] F.C. Asogwa, U.D. Izuchukwu, H. Louis, C.C. Eze, C.M. Ekeleme, J.A. Ezugwu, A. S. Adeyinka, Synthesis, characterization and theoretical investigations on the molecular structure, electronic property and anti-trypanosomal activity of benzenesulphonamide-based carboxamide and its derivatives, Polycycl. Aromat. Compd. (2022) 1–20.
[62] A.I. Ikeuba, A.U. Agobi, L. Hitler, B.J. Omang, F.C. Asogwa, I. Benjamin, M. C. Udoinyang, Green approach towards corrosion inhibition of mild steel during acid pickling using chlorpheniramine: experimental and DFT study, Chem. Afr. (2022) 1–15.
[63] H. Louis, M. Patrick, I.O. Amodu, I. Benjamin, I.J. Ikot, G.E. Iniama, A.S. Adeyinka, Sensor behavior of transition-metals (X= Ag, Au, Pd, and Pt) doped Zn11-X-O12 nanostructured materials for the detection of serotonin, Mater. Today Commun. (2022), 105048.
[64] Y. Wang, L. Wang, F. Zhang, N. Wang, Y. Gao, Y. Xiao, Y. Bao, Structure analysis and insight into hydrogen bond and van der waals interactions of etoricoxib cocrystals and cocrystal solvate, J. Mol. Struct. 1258 (2022), 132665.
[65] R.F. Bader, C.F. Matta, Atoms in molecules as non-overlapping, bounded, space-filling open quantum systems, Found. Chem. 15 (3) (2013) 253–276.
[66] C. Gharbi, H. Louis, I.O. Amodu, I. Benjamin, W. Fujita, C.B. Nasr, L. Khedhiri, Crystal structure analysis, magnetic measurement, DFT studies, and adsorption properties of novel 1-(2, 5-dimethyphenyl) piperazine tetrachlorocobaltate hydrate, Mater. Today Commun. (2022), 104965.
[67] S.A. Adalikwu, H. Louis, H.O. Edet, I. Benjamin, T.C. Egemonye, E.A. Eno, A. S. Adeyinka, Detection of hydrogen fluoride (HF) gas by Mg12O11-X (X= S, P, N, and B) nanosurfaces, Chem. Phys. Impact 5 (2022), 100129.
[68] X. Wu, J. Shen, H. Cao, M. Yuan, T. Ye, C. Lin, F. Xu, Theoretical sight into hydrogen bond interactions between arsenious acid and thiols in aqueous and HEPES solutions, J. Mol. Liq. 344 (2021), 117713.
[69] T. Lu, Q. Chen, Interaction region indicator: a simple real space function clearly revealing both chemical bonds and weak interactions, Chemistry Methods 1 (5) (2021) 231–239.
[70] D.N. Rodrigues, P.R. Olivato, P.R. Batista, L.C. Ducati, M. Dal Colle, Spectroscopic and theoretical studies of some 2-(2′-ethylsulfanyl) acetyl-5-substituted furans and thiophenes, J .Mol. Struct. 1261 (2022), 132895.
[71] G. Dong, K. Zhao, L. Zhang, Carbon self-doping induced high electronic conductivity and photoreactivity of gC 3N 4, Chem. Commun. 48 (49) (2012) 6178–6180.
[72] M.U. Khan, M.Y. Mehboob, R. Hussain, R. Fatima, M.S. Tahir, M. Khalid, A.A. C. Braga, Molecular designing of high-performance 3D star-shaped electron acceptors containing a truxene core for nonfullerene organic solar cells, J. Phys. Org. Chem. 34 (1) (2021) e4119.
[73] E.P. Nguyen, B.J. Carey, J.Z. Ou, J. van Embden, E.D. Gaspera, A.F. Chrimes, T. Daeneke, Electronic tuning of 2D MoS2 through surface functionalization, Adv. Mater. 27 (40) (2015) 6225–6229.
[74] C.O. Ehi-Eromosele, B.I. Ita, E.E.J. Iweala, Silica coated LSMO magnetic nanoparticles for the pH-Responsive delivery of 5-Fluorouracil anticancer drug, Colloids Surf. A 530 (2017) 164–171, https://doi.org/10.1016/j.colsurfa.2017.07.059.
[75] X. Wang, M. Salari, D.E. Jiang, J. Chapman Varela, B. Anasori, D.J. Wesolowski, Y. Gogotsi, Electrode material–ionic liquid coupling for electrochemical energy storage, Nat. Rev. Mater. 5 (11) (2020) 787–808.